Journal of Magnetic Resonance 212 (2011) 344–354

Contents lists available at SciVerse ScienceDirect

Journal of Magnetic Resonance

journal homepage: www.elsevier.com/locate/jmr

Optimising time-varying gradient orientation for microstructure sensitivity in diffusion-weighted MR

Ivana Drobnjak *, Daniel C. Alexander

Center for Medical Image Computing, Department of Computer Science, University College London (UCL), Gower Street, London WC1E 6BT, UK

ARTICLE INFO

Article history:
Received 12 April 2011
Revised 16 July 2011
Available online 29 July 2011

Keywords:
Axon diameter
Microstructure imaging
Generalized gradient waveform
Diffusion MR
Oscillating gradients
Pore size
PGSE
OGSE
Double-PGSE
Double wave vector

ABSTRACT

Here we investigate whether varying the diffusion-gradient orientation during a general waveform single pulsed-field gradient sequence improves sensitivity to the size of coherently oriented pores over having a fixed orientation. The experiment optimises the shape and the orientation of the gradient waveform in each of a set of measurements to minimise the expected variance of estimates of the parameters of a simple model. A key application motivating the work is measuring the size of axons in white matter. Thus, we use a two compartment white matter model with impermeable, single-radius cylinders, and search for waveforms that maximise the sensitivity to axon radius, intra-cellular volume fraction and diffusion constants. Output of the optimisation suggests the only benefit of allowing the gradient orientation to vary in the plane perpendicular to the cylinders is that we can gain perpendicular gradient strength by maximising two orthogonal gradients simultaneously. This suggests that varying orientation in itself does not increase the sensitivity to model parameters. On the other hand, the variation in a plane containing the parallel direction increases the sensitivity significantly because parallel sensitivity improves the diffusion constant estimates. However, we also find that similar improvement in the estimates can be achieved without optimising the orientation, but by having one measurement in the parallel and the rest in the perpendicular direction. The optimisation searches a very large space where it cannot hope to find the global minimum so we cannot make a categorical conclusion. However, given the consistency of the results in multiple reruns and variations of the experiments reported here, we can suggest that for probing coherently oriented systems, pulse sequences with variable orientation, such as double-wave vector sequences, do not offer more advantage than fixed orientation sequences with optimised shape. The advantage of varying orientation is however likely to emerge for more complex systems with dispersed pore orientation.

© 2011 Elsevier Inc. All rights reserved.

1. Introduction

Diffusion weighted MR is a non-destructive probe into the microstructure of materials, and can provide insight into pore morphology and fluid transport [1]. The technique is therefore useful for studying porous structures such as sandstone rocks, catalysts, and biological tissues [2–5]. Here we focus on biomedical applications, where diffusion MRI offers the potential to map microstructural features in tissue [6–9]. For example, in nervous tissue such as white matter in the brain, axon radius helps determine the conduction velocity [10,11] and hence changes in axon radius affect the nerve function. Thus imaging axon radius is a key challenge [6–8] as a reliable technique could provide insight into variations in cognitive performance within the general population and neuronal diseases that alter axon radius distribution, such as autism [12,13], amyotrophic lateral sclerosis (ALS) [14,15] or schizophrenia [16,17].

The choice of diffusion MRI pulse sequence and its parameters affect the sensitivity of diffusion MRI signal to the microstructure [18,19,9,20–22]. The standard pulsed gradient spin-echo sequence (PGSE) has been used with great success in animals and in vitro tissue [6–8,23,24], on water diffusing between beads [25], phantoms [26], and water diffusing between two infinite glass planes [27], but these approaches do not translate easily to humans due to the need for strong gradient strengths and long acquisition times. By carefully choosing the combination of PGSE settings, Alexander et al. got promising results on a human scanner with 0.06 T/m, but lack precision in estimates of the size of smaller axons (radii less than 3 μm) [28]. Alternative gradient waveforms, such as oscillating gradient spin-echo (OGSE) [29,9,20,21] or chirped [30], that contain a range of frequencies may provide greater sensitivity to smaller pore sizes. Drobnjak et al. [19] used optimisation techniques to identify the optimal shape of the generalised gradient waveform for the maximum sensitivity to the microstructure

* Corresponding author. Fax: +44 (0)20 7387 1397.
E-mail address: i.drobnjak@cs.ucl.ac.uk (I. Drobnjak).

1090-7807/$ - see front matter © 2011 Elsevier Inc. All rights reserved.
doi:10.1016/j.jmr.2011.07.017

parameters of a simple white matter model. They found, in simulation, that optimisation of the shape of the gradient waveform improves sensitivity to model parameters for both human and animal MR systems. In particular, the optimised waveforms made axon radii smaller than 3 μm more distinguishable than rectangular waveforms.

One limitation of the pulse sequence model in [19] is that the gradient orientation is fixed within each waveform. Variable orientation of the diffusion gradient, such as that in double-PGSE sequence [31], may provide additional sensitivity to pore sizes [32–36]. The double-PGSE sequence (double-wave-vector sequence) involves two consecutive PGSE blocks, each with a pair of diffusion gradients. The two pairs of gradients can have any angle between them and are separated by a mixing time. The sequence is primarily intended to probe microscopic anisotropy in macroscopically isotropic samples (such as the grey matter), where the single-PGSE sequence lacks sensitivity [32,37,38]. The technique has also been used to probe sizes of oriented pores [36,33], and others e.g. [32,35] suggest a potential advantage over the single-PGSE even in these systems. Shemesh et al. [39] do show an advantage of double-PGSE over single-PGSE using lower gradient strength. Specifically, they estimate oriented pore sizes with similar precision from both sequences, but using lower gradient strength in the double-PGSE. However it is not clear whether that advantage comes from the different shape of the waveform between the two sequences or specifically from varying gradient orientation in the double-PGSE. Drobnjak et al. [40] consider spiral waveforms, but they use it largely as a demonstration of their signal model. Thus the wider space of pulse sequences with varying orientation remains largely unexplored and their influence and benefit is not well known.

Here we use a stochastic optimisation procedure to search for the combination of varying-orientation gradient waveforms that are most sensitive to microstructure parameters typical for the white matter. We use the optimisation framework developed in [19] that optimises an imaging protocol consisting of several measurements, each with their own gradient waveform, to maximise their sensitivity to the parameters of a simple white matter model that includes axon radius. The measurements use the same basic pulse sequence structure as the PGSE, but replace the rectangular pulses with a gradient waveform defined discretely by a sequence of values that are free to vary independently. In contrast to [19], however, here we allow the gradient orientation to vary arbitrarily throughout each waveform. The recent extension of the method to 3D in [40] enables this more general optimisation. Thus, each gradient vector component, i.e. G_x, G_y and G_z, is defined discretely and each point of each component is optimised independently. Experiments use the same simplified-CHARMED model as in [18] and, in simulation, compare the sensitivity of optimised protocols with varying gradient orientation to those with fixed orientation. Amongst others, we consider cases when orientation is allowed to vary in the x–y plane (perpendicular to the white matter fibres), the x–z plane (parallel to the white matter fibres) and freely in x, y and z.

We start with the outline of the tissue and signal model together with the optimisation framework in Section 2. Experiments follow, which compare sensitivity to model parameters, over a range of axon radii, of optimised protocols with various constraints on the gradient orientation in Sections 3 and 4. Finally, the Discussion summarises findings, highlights limitations, and suggests further work and applications.

2. Methods

This section first describes the model used to calculate the diffusion MR signal. It then describes the optimisation framework used to determine the gradient waveform.

2.1. Tissue model

The white matter tissue model which we use is described in [18]. It is a simplified-CHARMED model with two compartments (hindered and restricted), with a single axon radius and assuming cylindrical symmetry of the apparent diffusion tensor in the extra cellular space. The model assumes parallel non-abutting cylindrical axon cells of fixed direction (along the z-axis), with equal radii and impermeable walls embedded in a homogenous extra-cellular medium. The parameters of the model are: the volume fraction $f \in [0,1]$ of the intra cellular compartment; the axon direction $\mathbf{n}$; the axon radius R; the intrinsic diffusion coefficient $d_{\|}$, which is the same in both compartments; and the apparent diffusion coefficient $d_{\perp}$. Ref. [18] gives a more complete description of the tissue model.

2.2. Pulse sequence model

The pulse sequence model has the same basic structure as the PGSE sequence, with two generalised (arbitrary) gradient waveforms in place of the two fixed rectangular pulses as Fig. 1 illustrates. The generalised gradient waveforms, $\mathbf{g}_o = [g_{ox}, g_{oy}, g_{oz}]$, are placed one on each side of the 180° RF pulse. Each component of the first one, $g_{ox}(n\tau)$, $g_{oy}(n\tau)$ and $g_{oz}(n\tau)$, $n = 1,\ldots,N$, is parametrized with N equally spaced points, and starts T_{prep} time after the 90° RF pulse is finished. The second one is the mirror reflection of the first. The full representation of the gradient in time is

$$\mathbf{g}(n\tau) = \begin{cases} 0 & 0 \leqslant n < N_1 \\ \mathbf{g}_o((n - N_1 + 1)\tau) & N_1 \leqslant n < N_1 + N \\ 0 & N_1 + N \leqslant n < N_1 + N + N_2 \\ \mathbf{g}_o((N_1 + 2N + N_2 - n)\tau) & N_1 + N + N_2 \leqslant n < N_1 + 2N + N_2 \\ 0 & N_1 + 2N + N_2 \leqslant n, \end{cases} \tag{1}$$

where $N_1 = integ((\mathrm{P90}/2 + T_{prep})/\tau)$ is the number of steps before the gradient starts[1], $N_2 = integ(\mathrm{P180}/\tau)$ is the number of steps during the 180° RF pulse and $N = integ((\mathrm{TE}/2 - \mathrm{P180}/2 - \mathrm{P90}/2 - T_{prep})/\tau)$ is the number of steps during one gradient waveform, n is an integer, TE is the echo time, P90 and P180 are respective durations of the 90° and 180° RF pulses, and τ is a fixed time interval.

2.3. Signal model

We write the diffusion MR signal

$$E = fE_r + (1 - f)E_h, \tag{2}$$

where E_r and E_h are normalised MR signals coming from the restricted (intra-cellular) and the hindered (extra-cellular) compartments respectively [41]. The hindered diffusion produces a Gaussian displacement distribution so that [42,43]:

$$E_h = \exp\left(-\gamma^2 D_h \int_0^{\mathrm{TE}} \left| \int_0^t \mathbf{g}_{eff}(t')\mathrm{d}t' \right|^2 \mathrm{d}t\right), \tag{3}$$

where $D_h = (d_{\|} - d_{\perp})\mathbf{n}\mathbf{n}^T + d_{\perp} I$ is the apparent diffusion tensor in the extracellular space, I is the identity tensor, and $\mathbf{g}_{eff}(t')$ is the effective time-dependent gradient waveform (the same as $\mathbf{g}(t')$ just with the reversed sign of the gradient vector after the 180° pulse) and γ is the gyromagnetic ratio.

To estimate the diffusion signal from the restricted compartment E_r, we use the matrix formalism method originally developed by Callaghan [44,45], and extended for gradient waveforms with time-varying orientation in [40].

[1] *integ* rounds to the nearest integer.

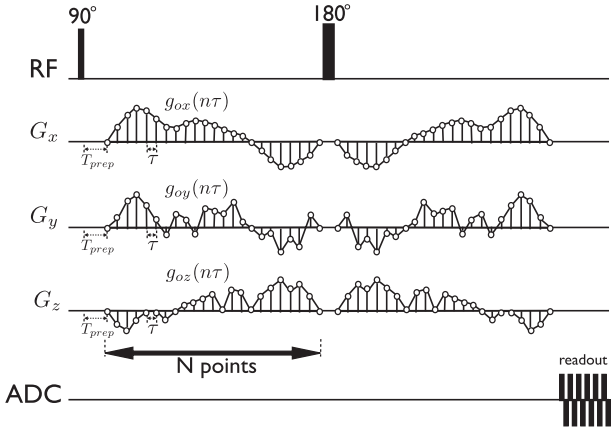

Fig. 1. Schematic representation of the sequence with generalised gradient waveforms for all three components G_x, G_y and G_z. The generalised gradient waveforms are mirrored about the 180° RF pulse, and amplitudes $g_{ox}(n\tau)$, $g_{oy}(n\tau)$, and $g_{oz}(n\tau)$, $n = 1,\ldots,N$ are optimised to give any shape. Points on the waveforms are separated with equal time intervals τ.

2.4. The optimisation framework

This section sets out the framework for optimising the imaging protocol. The protocol consists of M measurements each with different discretised gradient waveforms $g_{ox,j}$, $g_{oy,j}$ and $g_{oz,j}$, $j = 1,\ldots,M$. We seek the $g_{kjn} = g_{ok,j}(n\tau)$, where $k = x, y, z$; $j = 1,\ldots,M$; $n = 1,\ldots,N$ that maximise sensitivity to the model parameters.

The objective function

$$F = \sum_{i=1}^{W} (J^{-1})_{ii}/w_i^2 \tag{4}$$

reflects the precision of the model parameter estimates, and is defined as the sum of normalised CRLBs, for the model parameters ω_i, $i = 1,\ldots,W$, where $(J^{-1})_{ii}$ is the CRLB for ω_i. Here $W = 4$ and the ω_i are f, D_r, D_h and a. The CRLB provides a lower bound on the variance of a fitted model parameter that often correlates closely with the true variance. We assume a Rician noise model; the full expression for the CRLB assuming the Rician noise is in [18].

To ensure feasibility of the sequence on standard scanners, the optimisation enforces gradient hardware constraints onto the waveform amplitudes g_{kjn}: maximum gradient strength $0 \leqslant |g_{kjn}| \leqslant |G_{max}|$, and the maximum slew rate $0 \leqslant |(g_{kjn} - g_{kjn-1})|/\tau \leqslant S_R$, where S_R is the slew rate. We enforce the maximum slew rate by setting the time interval $\tau > 2|G_{max}|/S_R$.

We use a stochastic optimisation algorithm, SOMA (self-organising migratory algorithm) [46] with population size of 50, 500 migrations and otherwise default settings, to perform the minimisation. The full optimisation runs SOMA five times and picks the result with the smallest final value of the objective function. The SOMA algorithm is parallelized using MATLAB distributed toolbox, and a standard run takes 5h on 16 processors.

We keep the same number of iterations in the optimisation process to that used in [19], as we make no attempt to find the global minimum, but to find sufficiently reproducible solutions that we can observe emerging patterns. Since we do not find the global minimum, we refer to the protocols and waveforms that the optimisation outputs as optimised rather than optimal to specify that they are suboptimal solutions. The protocol consists of $M = 4$ measurements, which matches the number of free parameters in the model. Previous work, e.g. [18], finds that increasing M beyond this minimum can give minor improvements. However, larger M does not tend to introduce new unique measurements, but rather simply adds repeats of those that appear at the minimum M to sample more important measurements more heavily. Since here we are primarily interested in which waveforms arise, we fix $M = 4$, which minimises the complexity of the optimisation. Further details about the optimisation framework are described in [19].

3. Experiments

This section describes the specific set of experiments that investigate whether variable orientation waveforms improve the sensitivity of the signal to the microstructure parameters compared to fixed orientation waveforms. We investigate several different cases with different constraints on the gradient orientation to determine which particular features contribute to the sensitivity. The section starts by defining several types of protocols with different gradient waveform constraints. We then describe the pulse sequence parameters and the model parameters we use in the experiments. Finally, we describe the model fitting procedure.

3.1. Gradient waveform orientation

We define five protocol classes:

1. Protocol M_{1-4}:$\mathbf{G} = (G_x, 0, 0)$. The orientation is fixed along the x-axis. This case is published in [19] and it serves as a benchmark. Here we investigate two protocols in this class with different maximum gradient settings: (A) $|G_x| \leqslant G_{max}$; (B) $|G_x| \leqslant \sqrt{2}G_{max}$. Case B enables a fairer comparison with the next class, which can achieve gradient magnitude of $\sqrt{2}G_{max}$ along the diagonal directions such as $x = y$.
2. Protocol M_{1-4}:$\mathbf{G} = (G_x, G_y, 0)$. The orientation varies only perpendicular to the fibres (in the x–y plane) and $|G_x| \leqslant G_{max}$, $|G_y| \leqslant G_{max}$.
3. Protocol M_{1-4}:$\mathbf{G} = (G_x, 0, G_z)$. The orientation varies in a plane parallel to the fibres (the x–z plane). We look at this case separately from the perpendicular one as they separate the diffusion process into: diffusion with restriction (along x) and diffusion without restriction (along z). Here also $|G_x| \leqslant G_{max}$, $|G_z| \leqslant G_{max}$.
4. Protocol M_{1-3}:$\mathbf{G} = (G_x, 0, 0)$, M_4:$G = (0, 0, G_z)$. The orientation is fixed along the x-axis for three, and fixed along the z-axis for one measurement in a similar way to [47]. We investigate two different maximum gradient settings: (A) $|G_x| \leqslant G_{max}$, $|G_z| \leqslant G_{max}$; (B) $|G_x| \leqslant \sqrt{2}G_{max}$, $|G_z| \leqslant \sqrt{2}G_{max}$. Case B provides a fair comparison with class 3 above in a similar way to class 1 case B.
5. M_{1-4}:$\mathbf{G} = (G_x, G_y, G_z)$. The orientation is allowed to vary anywhere in the x–y–z coordinate system. We investigate two different maximum gradient settings: (A) $|G_x| \leqslant G_{max}$, $|G_y| \leqslant G_{max}$, $|G_z| \leqslant G_{max}$; (B) $|G_x| \leqslant \frac{\sqrt{2}}{\sqrt{3}}G_{max}$, $|G_y| \leqslant \frac{\sqrt{2}}{\sqrt{3}}G_{max}$, $|G_z| \leqslant \frac{\sqrt{2}}{\sqrt{3}}G_{max}$. As usual, case B normalises the maximum achievable gradient strength in any direction for a fair comparison with the other classes.

In total, we investigate eight protocols, which separate in two groups that provide different kinds of comparison:

(A) Un-equal maximum $|\mathbf{G}|$: Different protocols have the same constraint on the gradient components, i.e. $|G_x| \leqslant G_{max}$, $|G_y| \leqslant G_{max}$ and $|G_z| \leqslant G_{max}$, but different maximum achievable gradient magnitude $|\mathbf{G}|$ (e.g. in class 1 case A: $|\mathbf{G}| \leqslant G_{max}$ and in class 2 case A: $|\mathbf{G}| \leqslant \sqrt{2}G_{max}$). This is a situation we have on the typical scanner, where the constraints are imposed on each component individually.

(B) Equal maximum $|\mathbf{G}|$: Different protocols have the same constraint $|\mathbf{G}| \leqslant \sqrt{2}G_{max}$, but different constraints on the different gradient components. This provides a fair comparison of pro-

tocols with different orientational constraints without giving preference to protocols with stronger maximum achievable gradient strength.

In the rest of the paper, when we refer to a specific protocol, we will refer to their descriptive name from this list above, e.g. protocol M_{1-4}:**G** = (G_x, 0, 0), *A* or protocol class 1 case A.

3.2. Parameters

3.2.1. Pulse sequence parameters

We take G_{max} = 0.04 T/m and slew rate S_R = 200 T/m/s, which is typical of current human systems. We fix TE = 0.08 s and set the SNR of the unweighted (no gradients) signal at 20. We set the rest of the parameters as in [19]. We use T_2 = 0.07 s, which is typical for

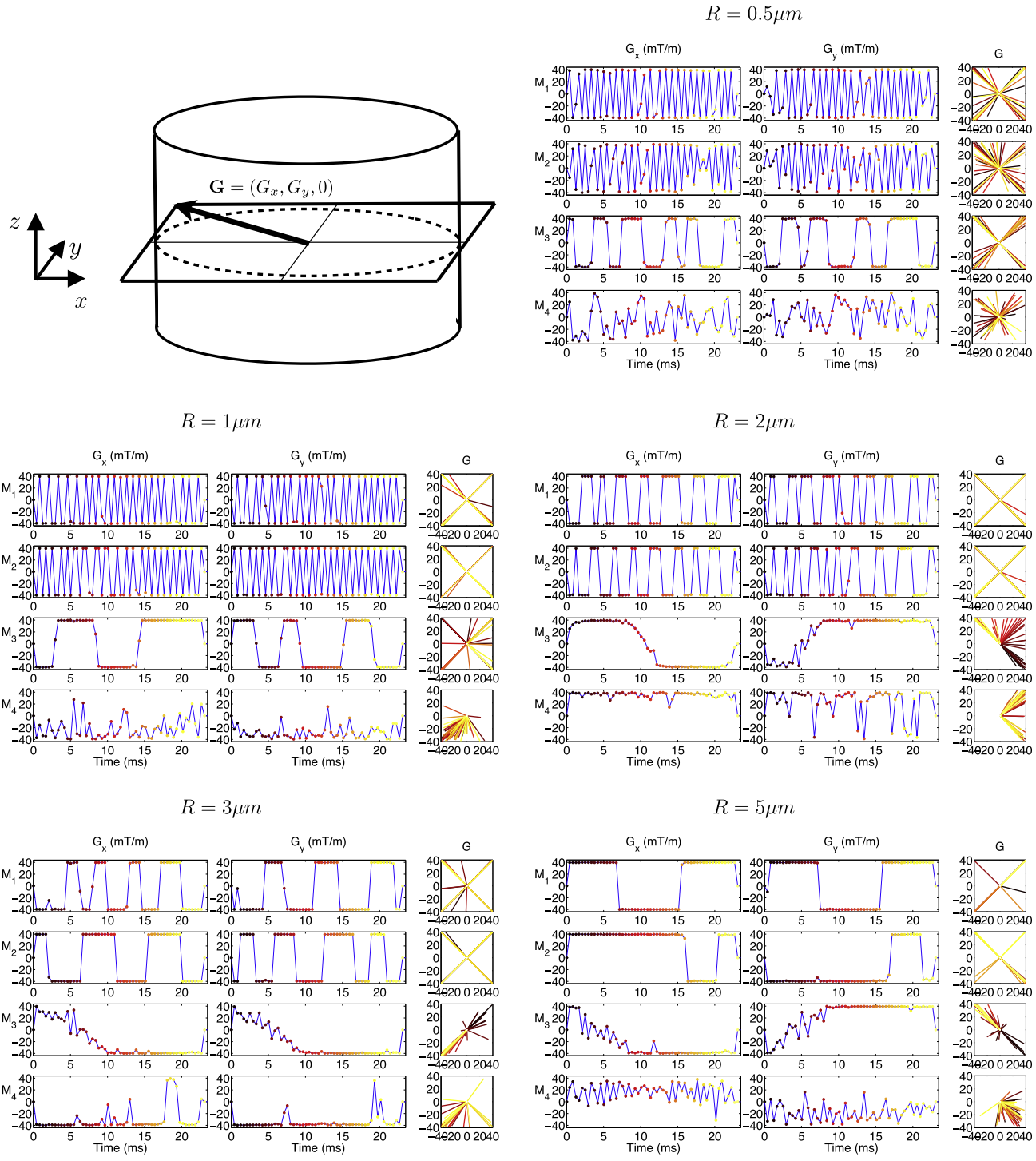

Fig. 2. Optimised gradient waveforms $\mathbf{g}_o(n\tau)$, $n = 1,\ldots,N$ for M_{1-4}:G = (G_x, G_y, 0), *A*. There are four measurements for each a-priori setting of radius *R*. The measurements are ordered with decreasing dominant frequency of oscillations, with the measurements of the highest dominant frequency in the top row. The position of vector **G** in the *x*–*y* plane is shown in the right-hand column of each subplot. The time points on the waveform are coloured (from black to white as the time progresses) and each vector is coloured with the colour of the corresponding time point.

white matter. Duration of the RF pulses and preparation time are P180 = 0.005 s, P90 = 0.0025 s, T_{prep} = 0.0059 s. The waveform unit-parameters τ = 0.00041 s and g_{step} = 0.0004 T/m are a couple of orders of magnitude smaller than the diffusion times and maximum gradient strength to ensure that the discrete waveform function is a good approximation of the continuous waveform. The time interval τ also satisfies $\tau \ll R^2/D_r$, making sure that the narrow pulse approximation is valid within each time interval.

3.2.2. Tissue model parameters

We assume δ-function priors on the model parameters: $f = 0.7$, $d_{\parallel} = 1.7 \times 10^{-9}$ m^2/s and $d_{\perp} = 1.2 \times 10^{-9}$m^2/s. We assume multiple δ-function priors on axon radius $R \in$ {0.5, 1, 2, 3, 5} μm, and optimise the protocol separately for each.

3.2.3. Estimating model parameters

The simple MCMC procedure in [18] provides samples of the posterior distributions of the model parameters given the data. We generate synthetic data using the optimised protocols of the cases outlined above. We add Rician noise to each measurement so that for the unweighted (no gradients) image SNR = 20. To fit the model, we assume 250 repeats of each of the four measurements with independent noise. We initialise the model parameters to their true value to speed up convergence.

4. Results

We present the results in three steps. We first show the optimised gradient waveforms in the optimised protocols for different classes outlined in Section 3. We then compare the sensitivity of the optimised protocols to model parameters by comparing the value of their respective objective functions. Finally, we compare the ability of the optimised protocols to recover model parameters by comparing posterior distributions.

4.1. Optimised generalised gradient waveforms

Optimised waveforms for protocol M_{1-4}:$G = (G_x, 0, 0)$, A are shown in [19]. Fig. 2 shows optimised gradient waveforms for protocol M_{1-4}:$G = (G_x, G_y, 0)$, A. Plots show waveforms $g_{ox}(n\tau)$ and $g_{oy}(n\tau)$, $n = 1, \ldots, N$ for each of the four measurements in the protocol. The optimised protocol is shown for each a-priori setting of radius R and the vector is shown for every time point $n\tau$ of the waveform $\mathbf{g}_o(n\tau)$.

Figs. 3 and 4 show the optimised waveforms for protocol M_{1-4}:$G = (G_x, 0, G_z)$, A and M_{1-4}: $G = (G_x, G_y, G_z)$, A. G_x and G_y waveforms are very similar to the G_x component in [19]. For M_{1-3}:$G = (G_x, 0, 0)$, M_4:$G = (0, 0, G_z)$, A the optimised waveforms of the first three measurements closely follow M_{1-4}:$G = (G_x, 0, 0)$, A while the fourth measurement follows the z-component of M_{1-4}: $G = (G_x, 0, G_z)$, A. All of the case B protocols closely follow their A counterparts, with adjusted gradient strengths data not shown.

As in [19], square-wave patterns with a range of frequencies emerge in all optimised protocols and the frequency of the square waves increases as radius decreases. These patterns arise for the non-zero G_x and G_y component for all protocols (Figs. 2–4). However, the G_z component does not have the square-wave pattern and fluctuates much more randomly.

We also observe that $\mathbf{G}$ tends to occupy the corners of the x–y plane, where the perpendicular gradient strength is the largest, in both M_{1-4}:$G = (G_x, G_y, 0)$ and M_{1-4}:$G = (G_x, G_y, G_z)$. The z-component tends less towards G_{max} and fluctuates fairly randomly over the range; see for example Fig. 3, where vector $\mathbf{G}$ sweeps both the left and the right side of the x–z plane. Similar observations can be made in Fig. 4.

Finally, Figs. 2–4 also show that the frequency of square-waves of the G_x and G_y components consistently decreases when the G_z component is introduced; compare for example Figs. 2 and 4.

4.2. Comparison of the objective functions

Fig. 5 shows the value of the objective function as a function of radius, R, for all optimised protocols. In the left plot we show results for case A: the un-adjusted maximum of $|\mathbf{G}|$, when $|G_k| \leqslant G_{max}$, $k = x, y, z$. In the right plot we show results for case B: the maximum of $|\mathbf{G}|$ is equal for all five classes and individual limits on each of the components appropriately adjusted (see Section 3).

In case A we obtain lower values of the objective function for protocol M_{1-4}:$G = (G_x, G_y, 0)$ compared to M_{1-4}:$G = (G_x, 0, 0)$, which suggests greater sensitivity to the model parameters. However, in case B these two classes have almost identical objective functions, suggesting that the main reason for their difference in case A is the maximum gradient strength, and that equating maximum achievable $|\mathbf{G}|$ renders their sensitivity the same.

On the other hand we obtain significantly lower values of the objective function for protocol M_{1-4}:$G = (G_x, 0, G_z)$ compared to M_{1-4}:$G = (G_x, 0, 0)$ in both cases A and B. These suggest that allowing orientation parallel to the fibres provides the lower value of the objective function.

The lowest value of the objective function is for M_{1-3}:$G = (G_x, 0, 0)$, M_4:$G = (0, 0, G_z)$. In case A due to the differences in the maximum gradient strengths this class lags behind M_{1-4}: $G = (G_x, 0, G_z)$ and M_{1-4}:$G = (G_x, G_y, G_z)$. However after normalisation in case B, it offers the lowest value of the objective function.

4.3. Comparing microstructure parameter estimates

Fig. 6, left column, shows the posterior distributions on radius R for optimised protocols (a) M_{1-4}:$G = (G_x, G_y, 0)$, B, (b) M_{1-4}:$G = (G_x, 0, G_z)$, B and (c) M_{1-3}:$G = (G_x, 0, 0)$, M_4:$G = (0, 0, G_z)$, B. All three protocols are of case B hence maximum achievable magnitude of the gradient $|\mathbf{G}|$ is equal for all three. The posterior distributions are markedly narrower for protocols with non-zero z-component as the objective function values suggest. The right column of the figure confirms these results, (b) and (c) produce more accurate (closer to the diagonal) and precise (smaller error bars) estimates compared to (a). Again following the trend of objective functions, we see from comparing (b) and (c) that protocol M_{1-4}:$G = (G_x, 0, G_z)$, B gives slightly less accurate and precise estimates than M_{1-3}:$G = (G_x, 0, 0)$, M_4:$G = (0, 0, G_z)$, B.

Fig. 7 shows the mean and standard deviation of posterior distributions on model parameters f, $d_{\parallel}$ and $d_{\perp}$ for optimised protocols (a) M_{1-4}:$G = (G_x, G_y, 0)$, B, (b) M_{1-4}:$G = (G_x, 0, G_z)$, B and (c) M_{1-3}:$G = (G_x, 0, 0)$, M_4:$G = (0, 0, G_z)$, B. The true values are marked with the straight line. The results for f and $d_{\perp}$ are relatively similar for all three protocols (protocol in (c) with slightly smaller error bars than the ones in (a) and (b)). However, the results for the intrinsic diffusion constant $d_{\parallel}$ are significantly better (estimates closer to the straight line and smaller error bars) for protocols with the parallel gradient component (b) and (c) compared to the protocol with only perpendicular components (a). The best estimates of $d_{\parallel}$ are achieved using protocol (c).

The optimised protocols for adjusted maximum magnitude protocol M_{1-4}:$G = (G_x, 0, 0)$, B produces very similar results to M_{1-4}:$G = (G_x, G_y, 0)$, B and M_{1-4}:$G = (G_x, G_y, G_z)$, B to those of M_{1-4}:$G = (G_x, 0, G_z)$. Results for the A cases (with non-adjusted maximum gradient magnitude) are the same as for the B cases, just proportionally better/worse to their differences in maximum gradient magnitude.

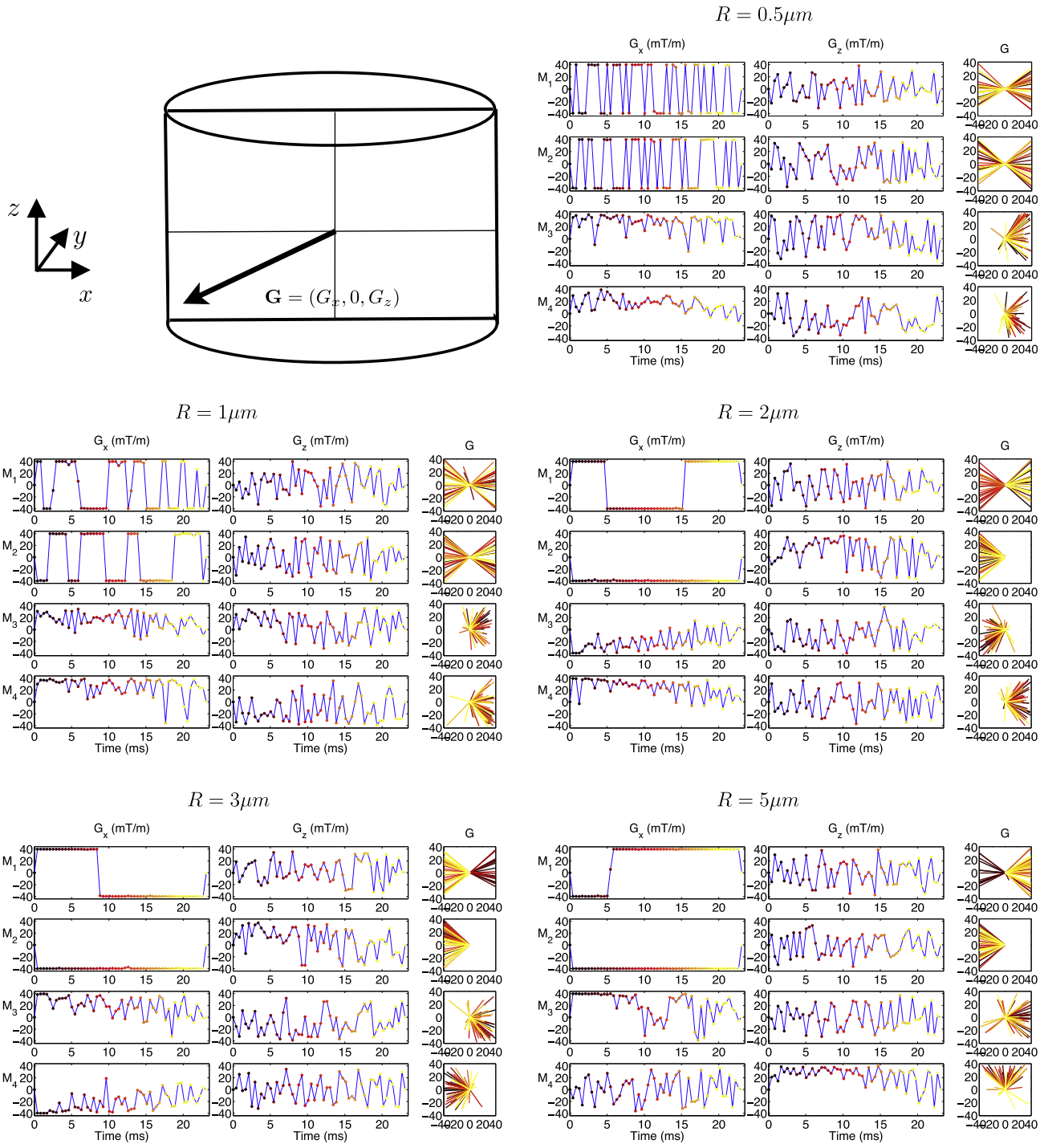

Fig. 3. As Fig. 2 for M_{1-4}:$G = (G_x, 0, G_z)$, A.

5. Discussion

Here we investigate whether variable orientation of the diffusion-gradients improves sensitivity to the size of coherently oriented pores over having a fixed orientation. We find that optimising the orientation of the gradient waveforms in the plane perpendicular to the cylindrical fibres (the x–y plane) does not increase sensitivity. On the other hand, optimising the orientation in the plane parallel to the cylindrical fibres (the x–z plane) does.

All three protocols that allow non-zero G_z provide very similar performance, although M_{1-3}:$G = (G_x, 0, 0)$, M_4:$G = (0, 0, G_z)$ performs slightly better than the others. Most likely this is simply because the optimisation for M_{1-3}:$G = (G_x, 0, 0)$, M_4: $G = (0, 0, G_z)$ takes less parameters so finds a better solution during the limited optimisation time. The observation supports the suggestion in [47] that adding a parallel measurement improves accuracy of fixed-direction axon diameter estimation techniques such as [6,7] that typically acquire only perpendicular measurements. It also helps explain why the ActiveAx orientationally invariant protocols in [18,28] are so successful despite ostensibly containing much less information than AxCaliber type fixed orientation protocols [6,7]. The key advantage is that the parallel measurement provides an

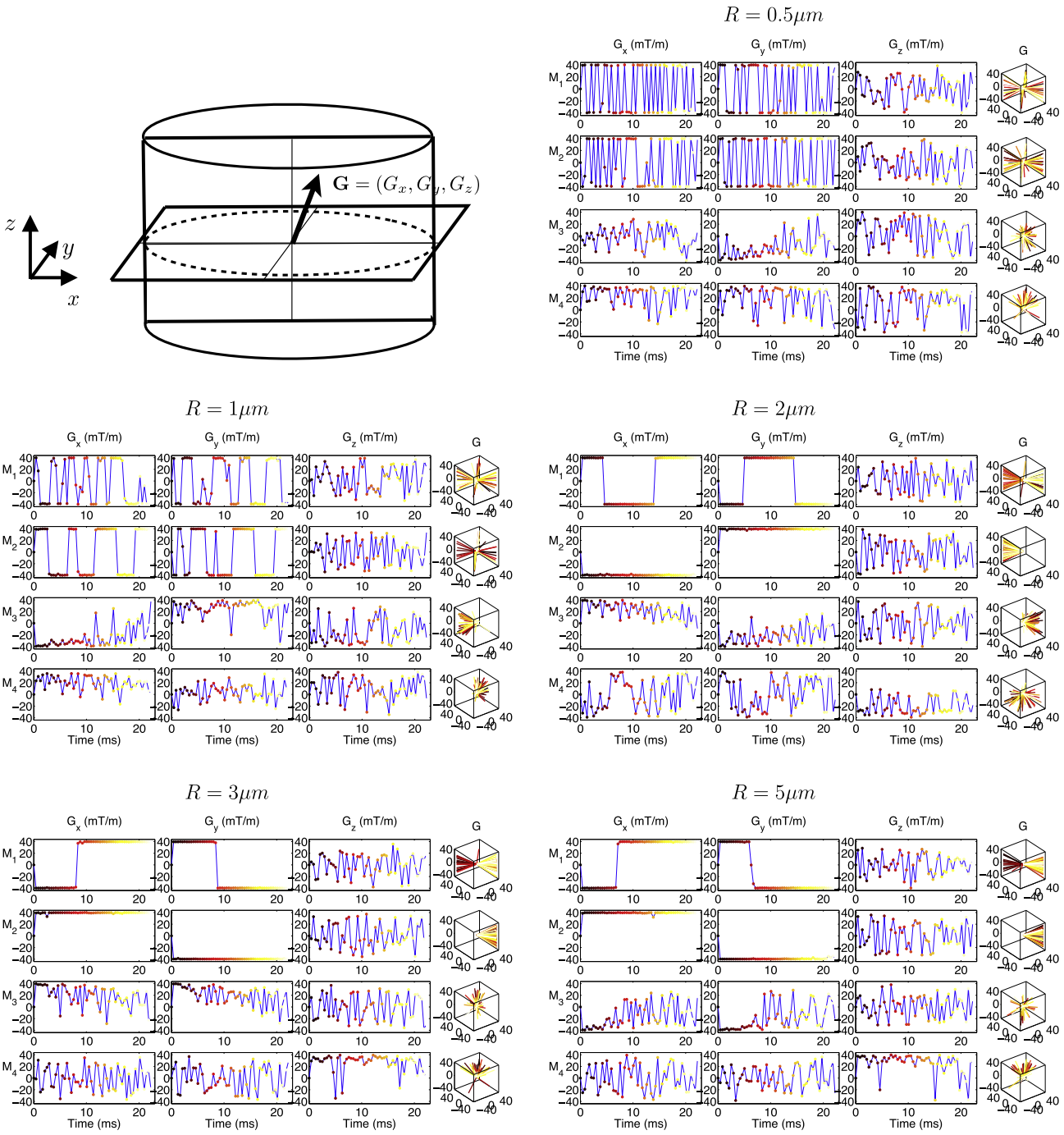

Fig. 4. As Fig. 2 for M_{1_4}:$G = (G_x, G_y, G_z)$, A except that the vector $\mathbf{G}$ in now shown in the x–y–z space in the right-hand column of each subplot.

independent estimate of the intrinsic diffusivity $d_{\|}$, which is much harder to estimate with a perpendicular gradient. The reduced frequency of oscillations in the protocols with non-zero G_z compared to those with $G_z = 0$ arise from the same effect. To estimate intrinsic diffusion constant $d_{\|}$ with a perpendicular gradient requires short diffusion time (high frequency) to minimise interaction with the restricting boundaries. However, once $d_{\|}$ is known from a parallel measurement where no restriction occurs, the remaining parameters can be estimated with lower frequencies. These effects reduce the minimum observable pore size for fixed G_{max}.

As expected, using more than one gradient component improves the results because each added component increases the maximum magnitude of the gradient. For example, the difference in the maximum magnitude between gradient vectors $\mathbf{G} = (G_x, 0, 0)$ and $\mathbf{G} = (G_x, G_y, G_z)$ is $\sqrt{3}$, which is sufficient to make the model parameter estimates significantly more accurate and precise.

The optimised, perpendicular to the fibres, waveforms G_x and G_y are very much alike, with square wave oscillations appearing consistently. They tend to be out of phase to allow the maximum $|\mathbf{G}|$ at the corners of the G_x–G_y square. The frequency of the waves increases as the radius decreases, as for the optimised protocols with fixed-orientation perpendicular, gradient waveforms in [19]. The optimised parallel waveforms G_z do not oscillate in the same way. Unlike G_x and G_y which mainly take $-G_{max}$ and G_{max} values, G_z takes the whole range of possible values in between fairly randomly. As discussed above, the G_z component is useful only to measure $d_{\|}$, which becomes a very simple experiment to estimate the diffusion coefficient for free diffusion. For that experiment, the

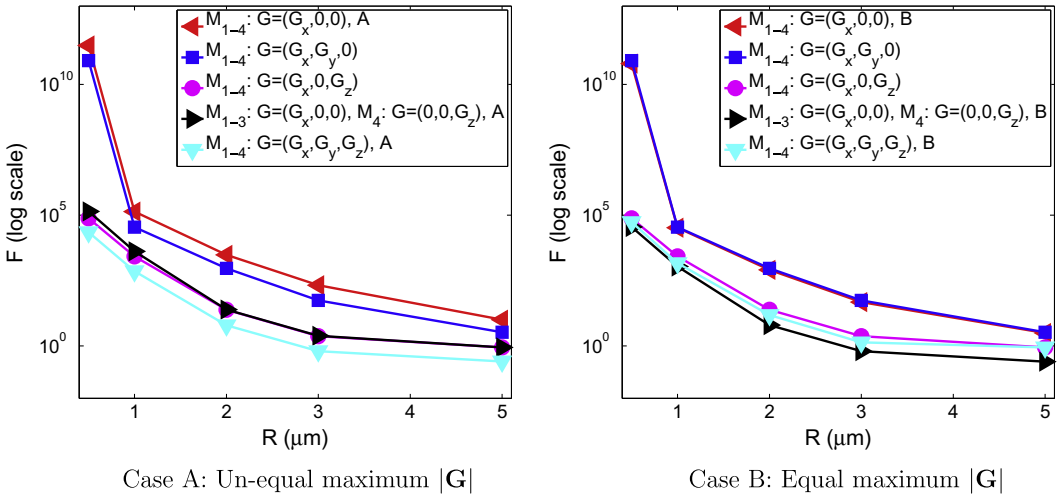

Case A: Un-equal maximum $|\mathbf{G}|$ Case B: Equal maximum $|\mathbf{G}|$

Fig. 5. Comparison of the objective function values of optimised gradient waveform protocols for all five different protocol classes for case A: $|G_k| \leqslant G_{max}$, $k = x, y, z$ and case B: $|\mathbf{G}| \leqslant \sqrt{2}G_{max}$.

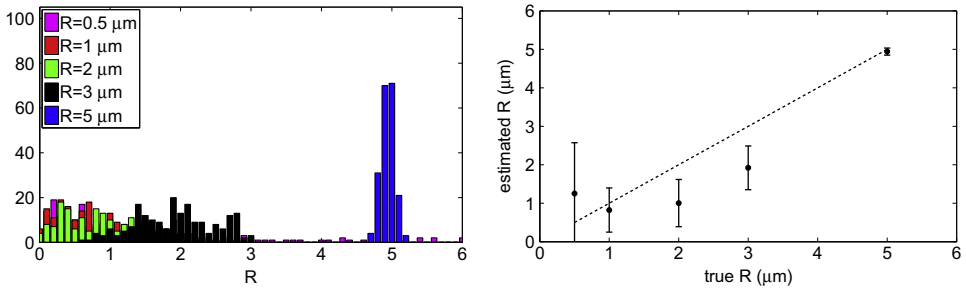

(a) $M_{1-4} : G = (G_x, G_y, 0), B$

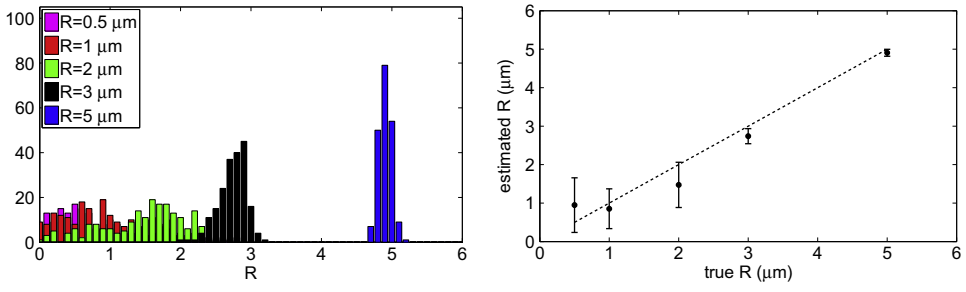

(b) $M_{1-4} : G = (G_x, 0, G_z), B$

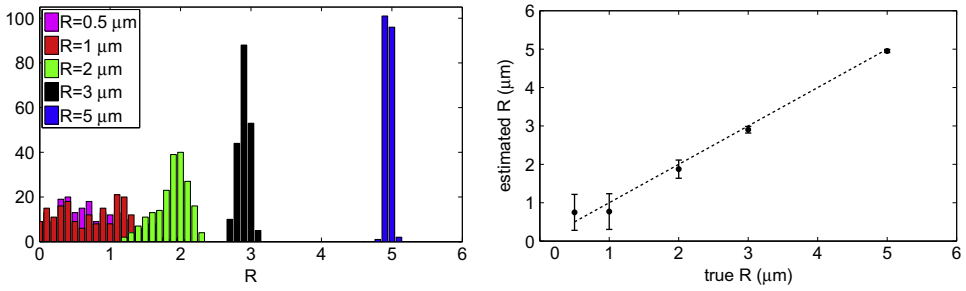

(c) $M_{1-3} : G = (G_x, 0, 0),\ M_4 : G = (0, 0, G_z), B$

Fig. 6. *Left column:* Posterior distributions on radius R (in μm) for optimised protocols (a) M_{1-4}:$G = (G_x, G_y, 0)$, B; (b) M_{1-4}:$G = (G_x, 0, G_z)$, B; and (c) M_{1-3}:$G = (G_x, G_y, 0)$, M_4:$G = (0, 0, G_z)$, B. The maximum gradient magnitude for all three protocols is equal. *Right column*: Mean and standard deviations of posterior distributions. The true values of the radii are on the diagonal.

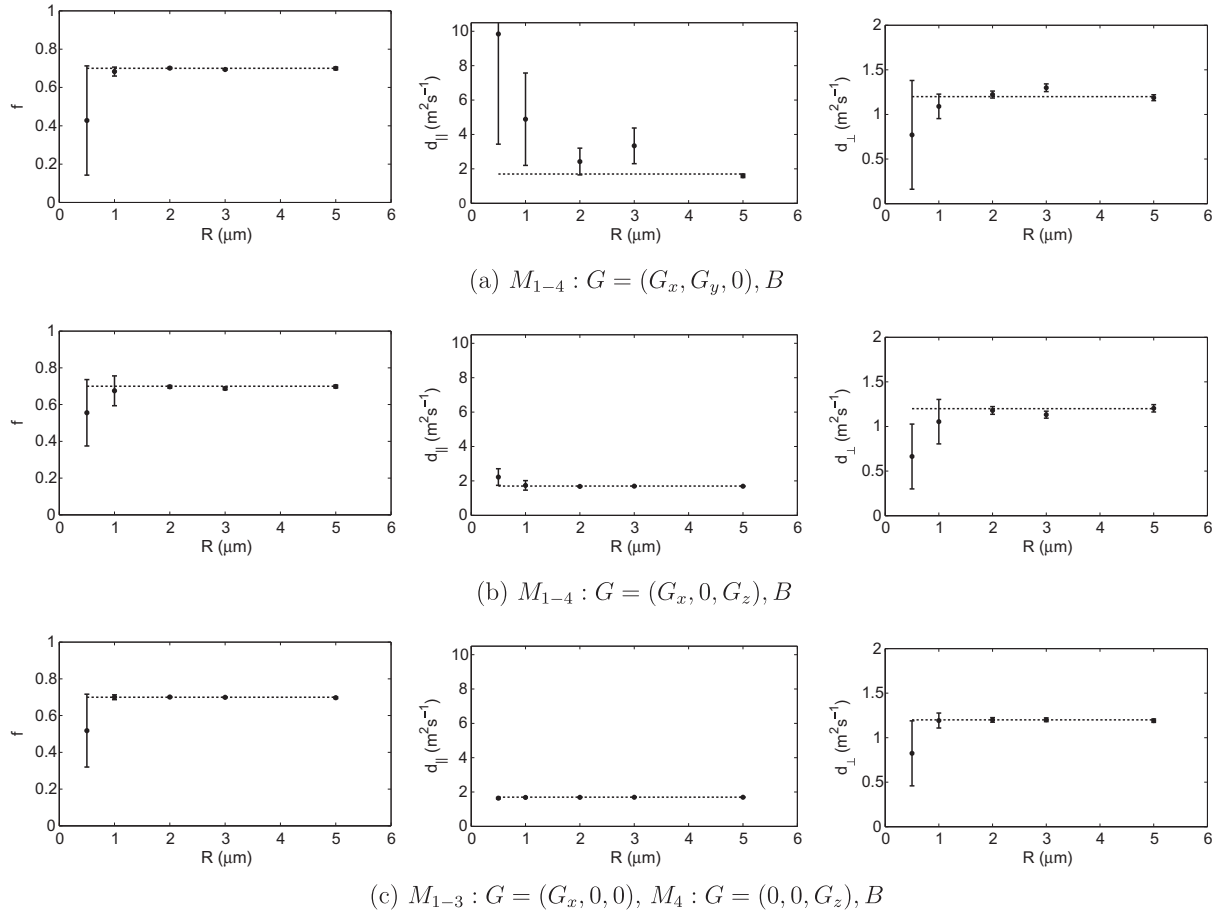

Fig. 7. Mean and standard deviations of posterior distributions on model parameters f, $d_{||}$, $d_{\perp}$ for optimised protocols (a) M_{1-4}:$G = (G_x, G_y, 0)$, B; (b) M_{1-4}:$G = (G_x, 0, G_z)$, B; and (c) M_{1-3}:$G = (G_x, G_y, 0)$, M_4:$G = (0, 0, G_z)$, B. The maximum gradient magnitude for all three cases is equal. The true values of the parameters are shown with dashed lines.

only important factor is the total diffusion weighting (the b-value) and the precise shape of the waveform has little effect (assuming fixed TE). The irregular shapes we observe are simply a random choice from many waveforms with a particular b-value. For example if we were to replace the z-direction waveform with a constant gradient having the same integral, the size estimation results would not change at all.

Overall the results here suggest that varying gradient orientation within single measurements offers no advantage for the simple system we are interrogating, i.e. the coherently oriented cylindrical pores. Although the optimised waveforms we obtain do have varying orientation, they show equivalent predicted (optimisation objective function value) and simulated (posterior variance on parameter estimates) performance to comparable waveforms with fixed orientation. Varying orientation appears in the waveforms because the precise choice of corner of the G_xG_y square or $G_xG_yG_z$ cube at any particular time point is somewhat arbitrary and many permutations of the different corners are equivalent. We note that the basic structure of the pulse sequence we use is that of a single-PGSE, however its generalised waveforms accommodate waveforms that reflect sequences like double-PGSE. However, the optimisation never finds such waveforms, which suggests they provide less sensitivity than straightforward oscillating gradients. The pulse sequence structure does not however accommodate stimulated echo sequences [48] or steady-state free procession [49]. We intend to extend the formulation in future to accommodate this wider class, but it seems unlikely the central conclusion, that varying orientation offers no advantage in estimating pore sizes in white matter like samples, will change with such an extension.

The advantage of varying orientation is however likely to emerge for more complex systems. Double-PGSE is designed for systems with anisotropic shaped pores, such as elliptical cylinders, or pores with dispersed orientation [32,50–53]. Future work will adapt the approach we use here for these systems where varying orientation should prove advantageous, and ultimately provide a tool for exploration of the broader gradient waveform space.

We must acknowledge the key conclusions here are not concrete, because the optimisation searches a very large space where it cannot hope to find the global minimum. Although we consistently find similar results in multiple reruns and variations of the experiments reported here, small pockets of the search space with varying orientation and smaller F may exist but remain unfound. Thus, our results only *suggest* that varying orientation offers no advantage for our simple white-matter model. Future work will compare with specific families of varying orientation pulse sequence, such as double-PGSE, to investigate this question further. However, a comprehensive search of the space of varying orientation waveform is likely to remain prohibitive.

Other areas for further work include adapting the optimisation for a more sophisticated and realistic white matter model. Here we focus on only the simplest model with parallel single-sized impermeable perfectly cylindrical pores and assumed Gaussian extracylindrical diffusion. The optimisation adapts naturally to models that include other parameters such as glial cell compartments [6,28], membrane permeability [6], a distribution of axon diameters [7], a distribution of axon orientations [53], pore anisotropy

[31,32,50], or better models of hindered diffusion, which may depart from Gaussian significantly at certain lengthscales [54].

We assume here a fixed and known fibre orientation. To generalise to unknown fibre orientation, we can adapt the optimisation and imaging protocol model to be similar to [18] where each waveform defines a high angular resolution diffusion imaging (HARDI) shell containing lots of measurements each with a unique central orientation. While conceptually simple, this adaptation increases computational requirements significantly, because we need to run the matrix method separately for each central orientation/waveform combination. However, that computation contains redundancy that potentially we can exploit to make the optimisation more manageable. Future work is required to explore this idea.

Finally, future work needs to verify the theoretical findings experimentally to begin translation to clinical implementation and practice. Measured signals will certainly depart from the theoretical predictions on which we base our objective function and optimisation, because of effects not included in our tissue and signal models. However, preliminary experimental results [55] do show good agreement between theoretical prediction and measured data with fixed orientation general waveforms and confirm the benefits for estimating the size of oriented pores. Furthermore, other groups recently implement more regular oscillating gradient waveforms successfully on a clinical scanner [56] with good results, so translation to clinical practice seems an achievable and promising prospect.

References

[1] P.T. Callaghan, A. Coy, T.P.J. Halpin, D. MacGowan, K.J. Packer, F.O. Zelaya, Diffusion in porous systems and the influence of pore morphology in pulsed gradient spin-echo nuclear magnetic resonance studies, J. Chem. Phys. 97 (1992) 651.

[2] A. Coy, P.T. Callaghan, Pulsed gradient spin-echo NMR diffusive diffraction experiments on water surrounding close-packed polymer spheres, J. Colloid Interface Sci. 168 (1994) 373–379.

[3] P.T. Callaghan, K.W. Jolley, J. Lelievre, Diffusion of water in the endosperm tissue of wheat grains as studied by pulsed field gradient nuclear magnetic resonance, Biophys. J. 28 (1979) 133–141.

[4] S. Godefroy, P. Callaghan, 2D relaxation/diffusion correlations in porous media, Magn. Reson. Imaging 21 (2003) 381–383.

[5] S. Umbach, E. Davis, J. Gordon, P. Callaghan, Water self-diffusion coefficients and dielectric properties determined for starch–gluten–water mixtures heated by microwave and by conventional methods, Cereal Chem. 69 (1992) 637.

[6] G.J. Stanisz, A. Szafer, G.A. Wright, R.M. Henkelman, An analytical model of restricted diffusion in bovine optic nerve, Magn. Reson. Med. 37 (1997) 103–111.

[7] Y. Assaf, T. Blumenfeld-Katzir, Y. Yovel, P.J. Basser, AxCaliber: a method for measuring axon diameter distribution from diffusion MRI, Magn. Reson. Med. 59 (2008) 1347–1354.

[8] D. Barazany, P. Basser, Y. Assaf, In vivo measurement of axon diameter distribution in the corpus callosum of rat brain, Brain 132 (2009) 1210–1220.

[9] J. Xu, M. Does, J. Gore, Sensitivity of MR diffusion measurements to variations in intracellular structure: effects of nuclear size, Magn. Reson. Med. 61 (2009) 828–833.

[10] J.B. Hursh, Conduction velocity and diameter of nerve fibers, Am. J. Physiol. 127 (1939) 1–139.

[11] J.M. Ritchie, On the relation between fibre diameter and conduction velocity in myelinated nerve fibres, Proc. R. Soc. London, B 217 (1982) 29–35.

[12] J. Piven, J. Bailey, B.J. Ranson, S. Arndt, An MRI study of the corpus callosum in autism, Am. J. Psychiat. 154 (1997) 1051–1056.

[13] J.R. Hughes, Autism: the first firm finding = underconnectivity?, Epilepsy Behav 11 (2007) 20–24.

[14] S. Cluskey, D.B. Ramsden, Mechanisms of neurodegeneration in amyotrophic lateral sclerosis, Mol. Pathol. 54 (2001) 386–392.

[15] T. Heads, M. Pollock, A. Robertson, W.H.F. Sutherland, S. Allpress, Sensory nerve pathology in amyotrophic lateral sclerosis, Acta Neuropathol. 82 (1991) 316–320.

[16] P.L. Randall, Schizophrenia, abnormal connection, and brain evolution, Med. Hypotheses 10 (1983) 247–280.

[17] D. Rice, S. Barone Jr., Critical periods of vulnerability for the developing nervous system: evidence from humans and animal models, Environ. Health Perspect. 108 (2000) 511–533.

[18] D.C. Alexander, A general framework for experiment design in diffusion MRI and its application in measuring direct tissue-microstructure features, Magn. Reson. Med. 60 (2008) 439–448.

[19] I. Drobnjak, B. Siow, D.C. Alexander, Optimizing gradient waveforms for microstructure sensitivity in diffusion-weighted MR, J. Magn. Reson. 206 (2010) 41–51.

[20] P.T. Callaghan, J. Stepisnik, Frequency-domain analysis of spin motion using modulated-gradient NMR, J. Magn. Reson., Ser. A 117 (1995) 118–122.

[21] J. Stepisnik, Analysis of NMR self-diffusion measurements by a density matrix calculation, Physica 104B (1981) 350–364.

[22] E. Özarslan, P.J. Basser, MR diffusion–"diffraction" phenomenon in multi-pulse-field-gradient experiments, J. Magn. Reson. 188 (2007) 285–294.

[23] H. Ong, A. Wright, S. Wehrli, A. Souza, E. Schwartz, S. Hwang, F. Wehrli, Indirect measurement of regional axon diameter in excised mouse spinal cord with q-space imaging: simulation and experimental studies, NeuroImage 40 (2008) 1619–1632.

[24] J. Latt, M. Nilsson, C. Malmborg, H. Rosquist, R. Wirestam, F. Stahlberg, D. Topgaard, S. Brockstedt, Accuracy of q-space related parameters in MRI: simulations and phantom measurements, IEEE Trans. Med. Imaging 26 (2007) 1437.

[25] P.T. Callaghan, A. Coy, D. MacGowan, K.J. Packer, F.O. Zelaya, Diffraction-like effects in NMR diffusion studies of fluids in porous solids, Nature 351 (1991) 467–469.

[26] L. Avram, Y. Assaf, Y. Cohen, The effect of rotational angle and experimental parameters on the diffraction patterns and micro-structural information obtained from q-space diffusion NMR: implication for diffusion in white matter fibers, J. Magn. Reson. 169 (2004) 30–38.

[27] D. Topgaard, O. Söderman, Experimental determination of pore shape and size using q-space NMR microscopy in the long diffusion-time limit, Magn. Reson. Imaging 21 (2003) 69–76.

[28] D.C. Alexander, P.L. Hubbard, M.G. Hall, E.A. Moore, M. Ptito, G.J. Parker, T.B. Dyrby, Orientationally invariant indices of axon diameter and density from diffusion MRI, NeuroImage 52 (2010) 1374–1389.

[29] E.C. Parsons Jr., M.D. Does, J.C. Gore, Temporal diffusion spectroscopy: theory and implementation in restricted systems using oscillating gradients, Magn. Reson. Med. 55 (2006) 75–84.

[30] A. Kiruluta, Probing restrictive diffusion dynamics at short time scales, J. Magn. Reson. 192 (2008) 27–36.

[31] D.G. Cory, A.N. Garroway, J.B. Miller, Applications of spin transport as a probe of local geometry, Polym. Prepr. 31 (1990) 149–150.

[32] P.P. Mitra, Multiple wave-vector extensions of the NMR pulsed-field-gradient spin-echo diffusion measurement, Phys. Rev. B 51 (1995) 15074–15078.

[33] M.A. Koch, J. Finsterbusch, Compartment size estimation with double wave vector diffusion-weighted imaging, Magn. Reson. Med. 60 (2008) 90–101.

[34] M.E. Komlosh, M.J. Lizak, F. Horkay, R.Z. Freidlin, P.J. Basser, Observation of microscopic diffusion anisotropy in the spinal cord using double-pulsed gradient spin echo MRI, Magn. Reson. Med. 59 (2008) 803–809.

[35] E. Özarslan, P.J. Basser, Microscopic anisotropy revealed by NMR double pulsed field gradient experiments with arbitrary timing parameters, J. Chem. Phys. 128 (2008) 154511.

[36] N. Shemesh, E. Özarslan, P.J. Basser, Y. Cohen, Measuring small compartmental dimensions with low-q angular double-PGSE NMR: the effect of experimental parameters on signal decay, J. Magn. Reson. 198 (2009) 15–23.

[37] N. Shemesh, Y. Cohen, Microscopic and compartment shape anisotropies in gray and white matter revealed by angular bipolar double-PFG MR, Magn. Reson. Med. 195 (2011) 153–161.

[38] M.E. Komlosh, F. Horkay, R.Z. Freidlin, U. Nevo, Y. Assaf, P.J. Basser, Detection of microscopic anisotropy in gray matter and in a novel tissue phantom using double pulsed gradient spin echo MR, J. Magn. Reson. 189 (2007) 38–45.

[39] N. Shemesh, E. Özarslan, M. Komlosh, P. Basser, Y. Cohen, From single-pulsed field gradient to double-pulsed field gradient MR: gleaning new microstructural information and developing new forms of contrast in MRI, NMR Biomed. 23 (2010) 757–780.

[40] I. Drobnjak, H. Zhang, M.G. Hall, D.C. Alexander, The matrix formalism for generalised gradients with time-varying orientation in diffusion NMR, J. Magn. Reson. 210 (2011) 151–157.

[41] Y. Assaf, R.Z. Freidlin, G.K. Rohde, P.J. Basser, New modeling and experimental framework to characterize hindered and restricted water diffusion in brain white matter, Magn. Reson. Med. 52 (2004) 965–978.

[42] E.O. Stejskal, J.E. Tanner, Spin diffusion measurements: spin echoes in the presence of a time-dependent field gradient, J. Chem. Phys. 42 (1965) 288–292.

[43] W.S. Price, Pulsed-field gradient nuclear magnetic resonance as a tool for studying translational diffusion: Part II. Experimental aspects, Concepts Magn. Reson. 10 (1998) 197–237.

[44] P.T. Callaghan, A simple matrix formalism for spin echo analysis of restricted diffusion under generalized gradient waveforms, J. Magn. Reson. 129 (1997) 74–84.

[45] S.L. Codd, P.T. Callaghan, Spin echo analysis of restricted diffusion under generalized gradient waveforms: planar, cylindrical, and spherical pores with wall relaxivity, J. Magn. Reson. 137 (1999) 358–372.

[46] I. Zelinka, SOMA-self-organizing migrating algorithm, in: B.V. Babu, G. Onwubolu (Eds.), New Optimization Techniques in Engineering, Springer.

[47] T. Schneider, C.A.M. Wheeler-Kingshott, D.C. Alexander, In-vivo estimates of axonal characteristics using optimized diffusion MRI protocols for single fibre orientation, in: Medical Image Computing and Computer-Assisted Intervention – MICCAI 2010, Lecture Notes in Computer Science, vol. 6361, Springer, Berlin/Heidelberg, 2010, pp. 623–630.

[48] K.D. Merboldt, W. Hanicke, J. Frahm, Diffusion imaging using stimulated echoes, Magn. Reson. Med. 19 (1991) 233–239.
[49] K.L. Miller, B.A. Hargreaves, G.E. Gold, J.M. Pauly, Steady-state diffusion-weighted imaging of in vivo knee cartilage, Magn. Reson. Med. 51 (2004) 394–398.
[50] E. Özarslan, Compartment shape anisotropy (CSA) revealed by double pulsed field gradient MR, J. Magn. Reson. 199 (2009) 56–67.
[51] M.A. Koch, J. Finsterbusch, Numerical simulation of double-wave vector experiments investigating diffusion in randomly oriented ellipsoidal pores, Magn. Reson. Med. 62 (2009) 247–254.
[52] N. Shemesh, E. Özarslan, T. Adiri, P.J. Basser, Y. Cohen, Noninvasive bipolar double-pulsed-field-gradient NMR reveals signatures for pore size and shape in polydisperse, randomly oriented, inhomogeneous porous media, J. Chem. Phys. 133 (2010) 044705.
[53] H. Zhang, P. Hubbard, G.J. Parker, D.C. Alexander, Axon diameter mapping in the presence of orientation dispersion with diffusion MRI, NeuroImage. 56 (2011) 1301–1315.
[54] M. Fonteijn, H.M. Hall, D. Alexander, The extracellular diffusion weighted signal predicts axon diameter distribution parameters, Proc. Intl. Soc. Mag. Reson. Med. (2010) 1563.
[55] B. Siow, I. Drobnjak, M. Lythgoe, D.C. Alexander, Optimised gradient waveform spin-echo sequence for diffusion weighted MR in a microstructure phantom, Proc. Intl. Soc. Mag. Reson. Med. (2011) 1966.
[56] D.J. McHugh, P.L. Hubbard, S. Zhao, D.M. Higgins, G.J. Parker, J.H. Naish, Probing tissue microstructure using oscillating diffusion gradients in the human calf, Proc. Intl. Soc. Mag. Reson. Med. 19 (2011) 1147.